Journal of Materials Chemistry C

ROYAL SOCIETY OF CHEMISTRY

COMMUNICATION

View Article Online
View Journal | View Issue

Check for updates

Cite this: J. Mater. Chem. C, 2020, 8, 10174

Received 4th June 2020,
Accepted 7th July 2020

DOI: 10.1039/d0tc02659j

rsc.li/materials-c

Published on 15 July 2020. Downloaded by Northwestern University on 9/27/2020 3:50:08 AM.

Thermoelectric transport of semiconductor full-Heusler VFe_2Al†

Shashwat Anand, Ramya Gurunathan, Thomas Soldi, Leah Borgsmiller, Rachel Orenstein and G. Jeffrey Snyder *

The full-Heusler VFe_2Al has emerged as an important thermoelectric material in its thin film and bulk phases. VFe_2Al is attractive for use as a thermoelectric materials because of it contains only low-cost, non-toxic and earth abundant elements. While VFe_2Al has often been described as a semimetal, here we show the electronic and thermal properties of VFe_2Al can be explained by considering VFe_2Al as a valence precise semiconductor like many other thermoelectric materials but with a very small band gap ($E_g = 0.03 \pm 0.01$ eV). Using a two-band model for electrical transport and point-defect scattering model for thermal transport we analyze the thermoelectric properties of bulk full-Heusler VFe_2Al. We demonstrate that a semiconductor transport model can explain the compilation of data from a variety of n and p-type VFe_2Al compositions assuming a small band-gap between 0.02 eV and 0.04 eV. In this small E_g semiconductor understanding, the model suggests that nominally undoped VFe_2Al samples appear metallic because of intrinsic defects of the order of $\sim 10^{20}$ defects per cm^{-3}. We rationalize the observed trends in weighted mobilities (μ_w) with dopant atoms from a molecular orbital understanding of the electronic structure. We use a phonon-point-defect scattering model to understand the dopant-concentration (and, therefore, the carrier-concentration) dependence of thermal conductivity. The electrical and thermal models developed allow us to predict the *zT versus* carrier concentration curve for this material, which maps well to reported experimental investigations.

1 Introduction

Heusler compounds are cubic structures with the general formula AMM'X where each element, typically all metals, makes a face-centered-cubic sublattice.[1] M and M′ are often the same element as in VFe_2Al. The resultant compound is usually metallic and considered an intermetallic compound.

There are also many half-Heusler compounds, with general composition AMX where M′ is vacant. Many half-Heusler compounds have been shown to be good thermoelectric semiconductors[2,3] where the semiconducting compositions are valence precise so that stable compositions and doping can be predicted using valence counting principles.[4,5] These materials exhibit extraordinary electrical properties[6] and thermal properties which can be engineered substantially through control of defects.[7–10] The thermoelectric figure of merit (zT) of both n-[11,12] and p-type[13–15] half-Heusler materials are comparable to that of state-of-the-art thermoelectrics. Additionally, these materials have superior mechanical properties[16,17] in comparison to well-known chalcogenide-based thermoelectrics, making them more advantageous for device applications.

The thermoelectric properties of the full-Heusler alloy composition of VFe_2Al has been studied extensively[18] because it is based on non-toxic, inexpensive and earth abundant elements, making it ideal for mass-produced, consumer products for waste heat recovery or refrigeration if sufficient thermoelectric efficiency can be achieved. The thermoelectric power factor of n-type bulk VFe_2Al[18,19] exceeds that of commercially available n-type Bi_2Te_3[20] at room temperature. Recently, remarkable thermoelectric properties were reported in films having the full-Heusler alloy composition of VFe_2Al, but with a metastable body centered cubic structure.[21] Both the high thermoelectric power factor and low thermal conductivity reported in the films[21] first warrant a better understanding of how the electronic structure of the full-Heusler bulk material leads to its thermoelectric transport properties.

Many full-Heusler compounds such as VFe_2Al appear to be stable with 24 valence electrons[1] per formula, which suggests there may be a molecular orbital explanation for the electronic structure and stability near a semiconducting composition as commonly found in Zintl phases[22] and half-Heusler thermoelectrics.[23] Nevertheless, in a majority of studies VFe_2Al has been interpreted as an indirect semimetal (see Fig. 1) with a pseudogap,[1,18,24,25] due to early photoemission[26], NMR[27] and computational[28–30] studies describing it as a semimetal.

Materials Science and Engineering, Northwestern University, Evanston, IL, 60208, USA. E-mail: jeff.snyder@northwestern.edu

† Electronic supplementary information (ESI) available. See DOI: 10.1039/d0tc02659j

This journal is © The Royal Society of Chemistry 2020

Published on 15 July 2020. Downloaded by Northwestern University on 9/27/2020 3:50:08 AM.

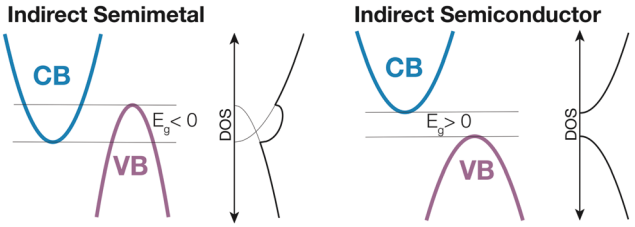

Fig. 1 Schematic demonstrating difference between electronic structure of indirect semimetals and semiconductors.

However, some properties of VFe_2Al are more consistent with a semiconductor (see Fig. 1) rather than a semimetal description.[31] For example, the nominally stoichiometric compound shows a decreasing electrical resistivity with increasing temperature, which is consistent with a semiconductor description.[26] The discrepancy between observed transport and semimetallic understanding of VFe_2Al has occasionally been rationalized using possible exotic phenomena such as 3d heavy fermion behavior.[26,30] However, subsequent heat capacity measurements do not appear to corroborate this behavior.[32] As a result, there is no general consensus on the band-gap and the observed transport properties in bulk VFe_2Al is poorly understood.

Here we review the thermoelectric properties of a variety of n and p-type VFe_2Al samples presented in the literature. We show that the experimental Seebeck coefficient, electrical resistivity and thermal conductivity as a function of temperature and doping is consistent with an interpretation of VFe_2Al as a small band-gap semiconductor with $E_g \approx 0.03 \pm 0.01$ eV rather than a semimetal. We attribute the past semimetalic interpretation of experimental data to the large concentration of intrinsic defects in the material which are present even in undoped VFe_2Al. This interpretation enables a modeling of the thermoelectric performance, including a prediction of maximum zT as well as engineering strategies for improving the thermoelectric properties that should be applicable to both bulk and thin film materials.

2 Results and discussion

2.1 Electronic structure

Depending on the level of theory used in the first-principles calculations, both semimetallic and semiconducting electronic structures have been reported[28–30,33–39] for VFe_2Al in the full-Heusler structure. In calculations showing the semimetallic bandstructure of VFe_2Al the hole and electron pockets lie in seperate high symmetry points (namely Γ and X respectively). The valence bands at Γ and the conduction band at X do not overlap in k-space but have the same energy over a 0.1 eV energy range so that the electronic structure can be described as a simple semimetal with negative band gap, $E_g \sim -0.1$ eV. In the case of semiconductor band structure reports, the bands look essentially the same with true valence bands at Γ and a conduction band at X but with predicted indirect band-gap (E_g) values >0.2 eV. Occasionally, the E_g values have been rationalized[33] using experimentally reported 'pseudogap'[24,27] in the electronic structure. However, in these experimental works a semimetallic electronic structure was still expected for VFe_2Al and the 'pseudogaps' were not representative of the indirect gap between X and Γ pockets.[24,27]

We calculate the electronic band structure of VFe_2Al using GGA+U calculations where the Hubbard U is selected to give a small band-gap E_g = 0.03 eV. We will show in the following sections that this small gap, rather than semimetallic $E_g \sim -0.1$ eV or the larger gap of $E_g > 0.1$ eV, is most consistent with the experimentally observed transport properties. The valence band maximum (VBM) is triply degenerate at the Γ point with a significant Fe character. The conduction band minimum (CBM), on the other hand, consists of a single band with V character at X due to highly dispersive V states. The valence and conduction bands have the same valley degeneracy of N_v = 3, since the single X-point pocket consists of 6 half-pockets in the Brillouin zone of this cubic structure.

The nature of the electronic bands can be rationalized using molecular orbital (MO) diagrams, which enables insight into the local bonding[23] and its effect on the valence and conduction bands in VFe_2Al. To construct the MO diagram (see Fig. 2b), we first determine the orbital character of all states at the Γ point using orbital projected partial density of states (pDOS) (see Fig. 3). Subsequently, we perform and a k-resolved Crystal Orbital Hamiltonian Population (COHP) analysis to investigate the nature[40] (bonding *versus* anti-bonding) and strength of interaction between these orbitals. In our analysis, we consider 4 conduction band

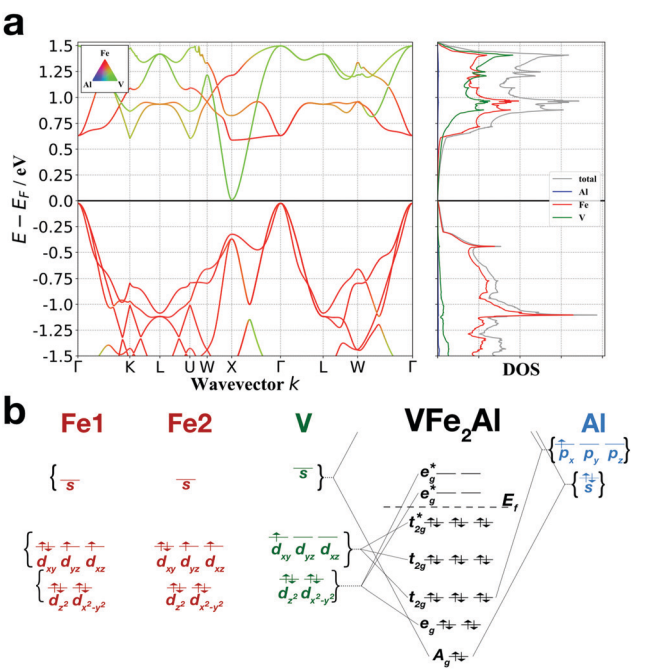

Fig. 2 (a) Atom resolved electronic band structure and density of states for VFe_2Al. (b) Schematic illustration of the molecular orbital diagram in VFe_2Al. The bonding (example e_g) and anti-bonding (example e_g*) interactions are concluded from partial density of states and k-resolved Crystal Orbital Hamilton Population (COHP) analysis of states at the G point in the electronic structure (see Fig. S1–S15, ESI†). States close to the Fermi-level (E_f) predominantly show e_g and t_{2g} character from V and Fe atoms.

Published on 15 July 2020. Downloaded by Northwestern University on 9/27/2020 3:50:08 AM.

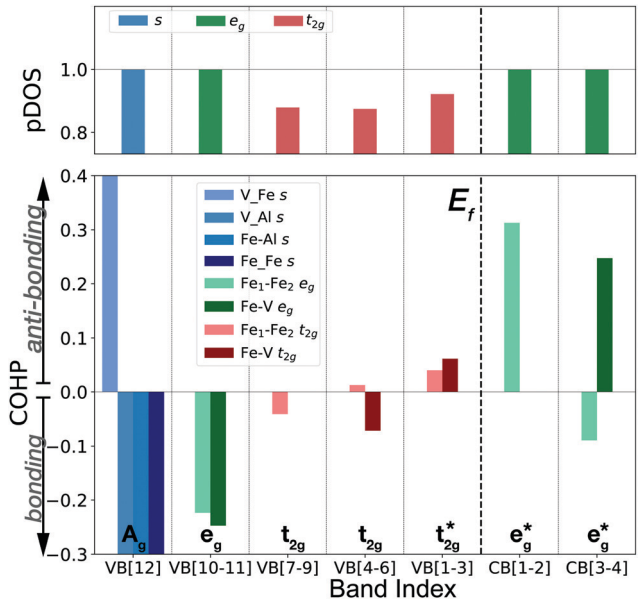

Fig. 3 Orbital projected partial Density of States (pDOS) and *k*-resolved Crystal Orbital Hamiltonian Population (COHP) of Γ-point states of VFe_2Al. The *x*-axis indicates the band index of the Γ-point state. The indices of the valence (VB) and conduction bands (CB) are counted with respect to the Fermi-level (E_f). Degenerate bands are indexed together. The pDOS are determined by adding contributions from s (blue bar), t_{2g}-type (d_{xy}, d_{yz}, d_{zx} red bars) and e_g-type ($d_{x^2-y^2}$, d_{z^2}, red bars) orbitals separately regardless of the atom type. pDOS value of 1 would mean complete contribution from a particular set. The COHP values were determined by averaging across all inter-atomic interactions between orbitals of the same type (for example averaging between Fe d_{z^2}–V d_{z^2} and Fe $d_{x^2-y^2}$–V $d_{x^2-y^2}$ COHP to obtain Fe–V e_g COHP). Negative and positive COHP values indicate bonding and anti-bonding interactions respectively. COHP value of zero indicates the absence of any interaction. In general, interaction strength increases as $t_{2g} < e_g < s$.

states and 12 valence band states each with an occupancy of 2. The valence bands chosen in our analysis contain all the 24 valence electron of the compound (8×2 from Fe, 5 from V and 3 from Al).

We find that, with the exception of the lowest valence band A_g, the valence band states and lowest conduction band states primarily arise from interactions between Fe and V d-states (see Fig. 3). Since, both Fe and V are surrounded by a tetrahedral environment, their d-orbitals split into t_{2g} (d_{xy}, d_{yz} and d_{zx}) and e_g (d_{z^2} and $d_{x^2-y^2}$) orbitals. The three sets of t_{2g} from V and the two Fe atoms interact to form three filled sets of t_{2g} molecular orbitals in the valence band. The three sets of e_g orbitals interact more strongly than the t_{2g} orbitals pushing two sets above the Fermi-level and only one set lower in the valence band. The relative interaction strength of t_{2g} and e_g orbitals can be seen from their magnitude of COHP values for the conduction and valence band states at the Γ point (see Fig. 2b and 3). Generally, the COHP values for e_g interactions are considerably larger than those due to t_{2g} interactions. The lowest valence band A_g in the molecular orbital diagram has a predominantly bonding s-orbital type character with almost equal contributions from all atoms in the compound (see Fig. 3 and Fig. S14, ESI†). The COHP of the A_g largely reveals a very strong bonding interaction between the s-orbitals, indicating that it originates from interactions between high energy s-orbitals of the compound (see Fig. 2b and 3).

In general, Al contribution to the valence band states is rather small. While the A_g and the lowest t_{2g} molecular orbitals show some Al contributions (see Fig. S14 and S10, ESI†), the content of Al s and p-states are less than 25% and ~5%, respectively. Among the three elements, Al is the most electropositive (Pauling electronegativity of 1.61) and the small Al content in the valence bands indicates that the Al can be treated as a Al^{3+} cation within a valence balanced description[5] of this semiconductor compound. With Fe as the most electronegative element, we assign the A_g states and the filled e_g states to Fe giving each 9 electrons or a valence of Fe^{1-}. V, on the other hand, only has its t_{2g} states filled totaling 6 electrons or V^{1-}. Thus the 24 electron/formula unit compound can be understood as valence balanced composition $V^{1-}Fe_2^{1-}Al^{3+}$.

The full-Heusler structure is very similar to that of half-Heusler compounds with just an additional transition metal atom M′ occupying the vacant sub-lattice in the structure. The molecular orbital picture of full-Heusler semiconductor allows for comparison with electronic structure of semiconductor half-Heusler compounds.[41] Similar to half-Heusler compounds, states on either side of the Fermi-level (E_f) in VFe_2Al are formed from transition metal d-states (see Fig. 2). In particular, the Γ point states of the first conduction and valence bands show d-orbital character from Fe atoms which constitute the M′ sub-lattice. Removing the M′ atom from the structure would presumably decrease the number of states close to the E_f and the d–d interaction between transition metal atoms, thereby opening up the band-gap. From this understanding one can explain the larger band-gaps generally observed in half-Heusler compounds when compared to full-Heusler compounds such as VFe_2Al and VFe_2Ga. The impact of adding atoms in the M′ sub-lattice of the half-Heusler structure has been studied for TiNiSn. Ni solubility in TiNiSn introduces mid-gap defect states which impact the thermoelectric properties of the material significantly.[9] The main difference between half-Heusler and full-Heusler semiconductors is the electronegativity of the X-atom. While Al is the most electropositive atom in VFe_2Al behaving as a 3+ cation, in half-Heusler NbFeSb the Sb atom is the most electronegative and acts as a 3− anion within the Zintl description of the compound.[5]

2.2 Mobility and effective mass

The trends in Seebeck coefficient S and electrical conductivity σ for VFe_2Al with temperature and doping are generally that expected from a small band gap semiconductor. With sufficient doping, the electrical properties are determined by one band, either the conduction or valence band. The weighted mobility (μ_w) of charge carriers in the dominant band can be determined from the variation of $|S|$ with σ[48,49] (see Section 4.2). Fig. 4a and b shows that μ_w for both electrons and holes is in the range from 250–700 $cm^2\ V^{-1}\ s^{-1}$, which is comparable to the best thermoelectric materials, Bi_2Te_3 based alloys.[20]

 This journal is © The Royal Society of Chemistry 2020

Published on 15 July 2020. Downloaded by Northwestern University on 9/27/2020 3:50:08 AM.

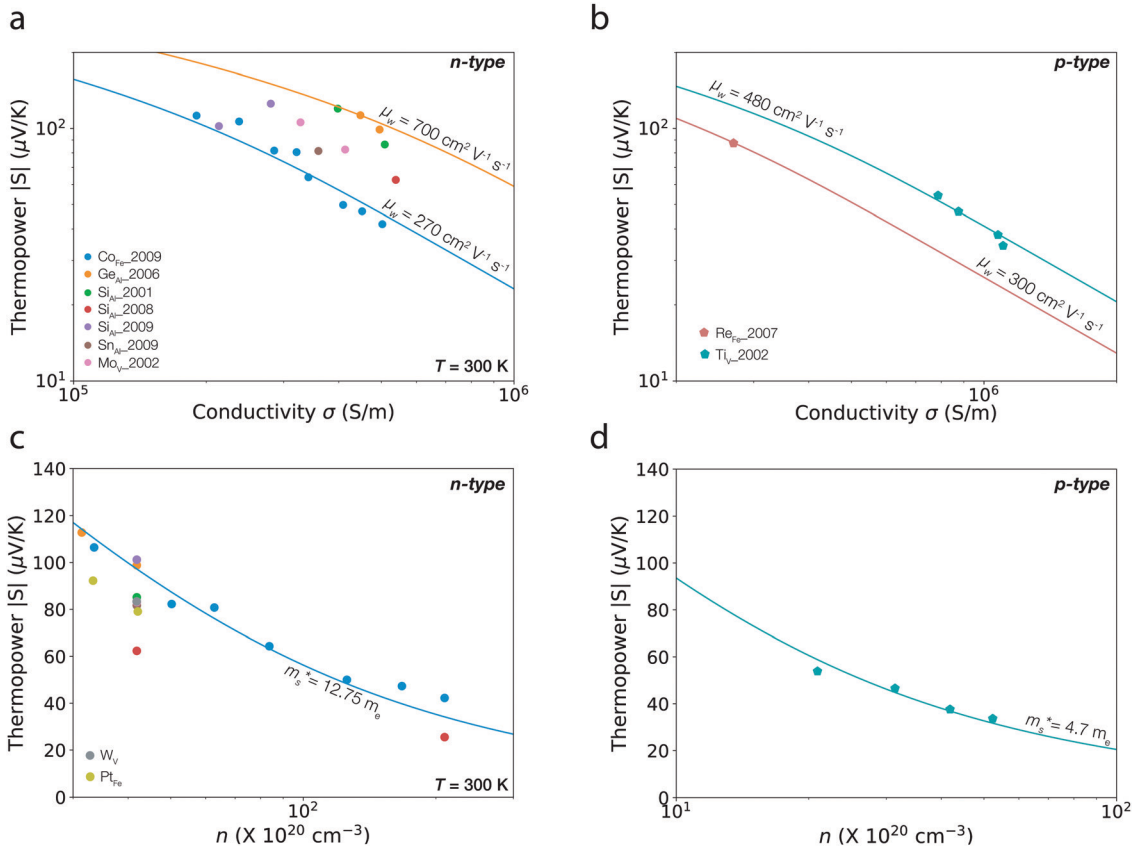

Fig. 4 Variation of thermopower (|S|) in VFe_2Al with different type and concentration of doping[18,19,42–47] at room temperature. (a and b) Plot of log|S|–log|σ| which gives the weighted mobility (μ_w) with n-type (a) and p-type (b) dopants. For both cases, the solid curves represent the prediction corresponding to constant values of μ_w. (c and d) Themopower *versus* carrier concentration (*n*) plot to determine the effective mass (m_s*) of n-type (c) and p-type (d) VFe_2Al samples (scatter points). The solid curves show the prediction for a constant *m** which fit reasonably well across the entire range of *n*.

The effective mass (m_s*), is determined from the dependence of Seebeck on carrier concentration (Fig. 4c and d, Section 4.2). Since Hall carrier concentration can be affected by magnetic impurities and is often not reported, we used the chemical carrier concentration (*n*) calculated from the nominal valence electron concentration that includes dopants in the samples.

The conduction band appears to be heavier with values of $m_s^* = 13m_e$ than the valence bands $m_s^* = 5m_e$, where m_e is the mass of an electron (see Fig. 4c and d). Such large m_s* values (density of states effective masses) are typical of half-Heusler compounds,[13,23] and could indicate multiple band effects particularly at higher carrier concentrations.[35]

The reported properties of different dopants in VFe_2Al give somewhat different values for μ_w, which could be due to differences in microstructure or changes in the bulk electronic properties. Weighted mobility values are known to be quite sensitive to grain boundaries and interfaces in some materials, such as half Heuslers,[50] which can be greatly altered depending on the synthesis conditions. Typically, samples with larger grain sizes tend to show larger μ_w. We believe that the variance in μ_w values of Si samples (400–650 $cm^2\ V^{-1}\ s^{-1}$) could be explained by such factors.

Changes to the bulk μ_w might be rationalized by considering the atomic contributions to conducting states in the electronic structure. Adding defects to atomic sites that contribute more to the conduction (valence) band are more likely to scatter electrons (holes) and reduce the n-type (p-type) μ_w, as demonstrated in thermoelectric PbSe.[51] For example, the higher $\mu_w = 480\ cm^2\ V^{-1}\ s^{-1}$ for Ti doping on the V site when compared to Re-doping on the Fe site ($\mu_w = 300\ cm^2\ V^{-1}\ s^{-1}$, see Fig. 4b) is expected because the valence band maximum is dominated by Fe states rather than V states. We further expect p-type samples with substitution on the Al site (*e.g.* Mg doping) to possibly show even higher μ_w. To the best of our knowledge, this has not yet been investigated. Similarly, a high μ_w for Si and Ge doped VFe_2Al is expected because these dopants should substitute on the Al site, which has little contribution to either conduction or valence band. Indeed the μ_w for Si and Ge doped VFe_2Al is generally higher than the μ_w for Mo and Co doping (also n-type) where Mo and Co are expected to substitute on the Fe or V site. Mo and Co doping could also change the localized spin state of the transition metals which could lead to spin-disorder scattering of electrons that reduce μ_w.[52]

2.3 Band-gap estimation

The effect on transport properties (electrical resistivity, Seebeck, Hall effect, electronic portion of thermal conductivity, *etc.*) due to having both electrons and holes (bipolar effect) can be used to

Published on 15 July 2020. Downloaded by Northwestern University on 9/27/2020 3:50:08 AM.

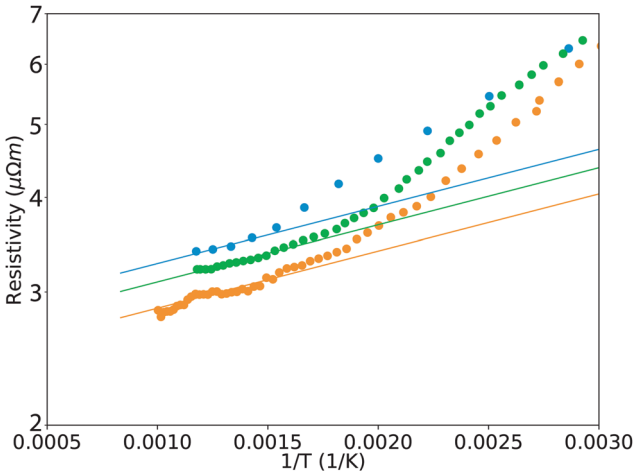

Fig. 5 Arrhenius plot for resistivity measurements of three undoped VFe_2Al samples (filled circles) from previous reports.[19,42,47] Slope of the solid lines correspond to a small band-gap of E_g = 0.03 eV.

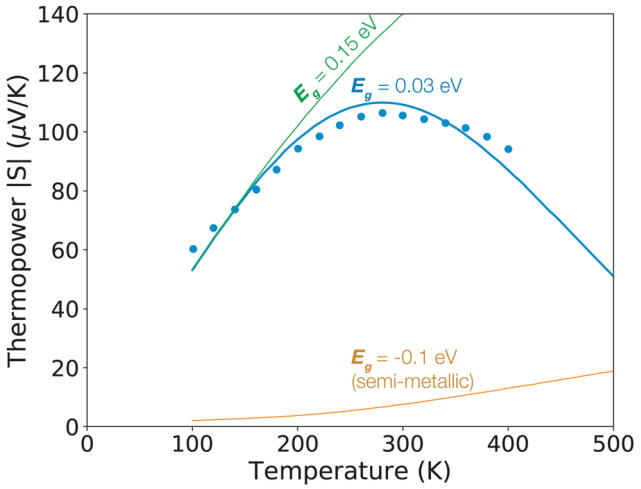

Fig. 6 Temperature dependence of Seebeck coefficient for VFe_2Al sample (scatter points) doped with 10% Mo.[46] Solid lines represent predictions from two-band acoustic phonon scattering models with E_g = 0.15 eV, 0.03 eV and −0.10 eV (semimetallic). The weighted mobility (μ_w) values used in these models for majority and minority carriers were 440 $cm^2\ V^{-1}\ s^{-1}$ and 480 $cm^2\ V^{-1}\ s^{-1}$ respectively. Observed temperature dependence of Seebeck coefficients for VFe_2Al can be best understood from a small gap semiconductor description of the compound.

estimate the band gap (or negative band gap for a semimetal). Although there is substantial variability in the reported samples and techniques to estimate band gap, the data, using three methods, are generally consistent with a positive band gap in the range of 0.02 eV to 0.04 eV.

A classic method to estimate band gap of a semiconductor is to examine the temperature dependent resistivity in the intrinsic regime. An Arrhenius plot of the high temperature resistivity data from three, previous reports on undoped VFe_2Al samples follows $\rho \propto \exp\left(\frac{E_g}{2k_B T}\right)$ suggesting E_g = 0.03 eV (see Fig. 5). Fitting the data at lower temperatures would give larger values for E_g, possibly explaining the value of 0.1 eV reported in a previous temperature dependent resistivity analysis.[26]

Another common method to estimate band gaps in thermoelectric materials is to use the Goldsmid-Sharp method[53] which examines the peak in thermopower $|S|$ as a function of temperature (Fig. 6) in a moderately doped semiconductor using $E_g \approx 2e|S_{max}|T_{max}$. For an accurate estimate, the ratio of the weighted mobility of the conduction and valence band is needed,[53] which have been estimated from the section above. Once again, we see that a small positive band gap with E_g = 0.03 eV fits much better than a large gap such as E_g = 0.15 eV or negative E_g = −0.1 eV (semimetal, see Fig. 6).

The bipolar effect is also noticeable in the low thermopower $|S|$ of lightly doped semiconductors. For example, the maximum thermopower observed just before or after the transition between p-type and n-type, as a function of doping (Fig. 7) also depends on the band gap and weighted mobility ratio. The μ_w and m_s^* values attained for electron and hole conduction in the previous section can be used to construct a two-band model to predict the Seebeck coefficient at any dopant concentration. The room temperature Seebeck data from a variety of compositions reported in the literature appears to peak around $\sim -140\ \mu V\ K^{-1}$ for n-type and $\sim +70\ \mu V\ K^{-1}$ for p-type which fits E_g = 0.02 eV in the two-band model well (see Fig. 7). Increasing E_g above ~0.1 eV gives a very poor fit (see Fig. 7). For example, a band-gap of 0.15 eV predicts maximum Seebeck values exceeding 200 $\mu V\ K^{-1}$, which is much larger than any observed value. Similarly, modelling the material as a semimetal with E_g = −0.1 eV predicts Seebeck values smaller than 50 $\mu V\ K^{-1}$ over the entire doping range. The two-band model uses μ_w values of 700 $cm^2\ V^{-1}\ s^{-1}$ for electrons and 300 $cm^2\ V^{-1}\ s^{-1}$ for holes based on the analysis of heavily doped materials above. The large ratio of μ_w values (>2) leads to the asymmetry in peak Seebeck values observed.

In early experimental reports, VFe_2Al has often been described as semimetal based on the observation of a measurable density of states at the Fermi-level.[26] Undoped VFe_2Al typically shows a low, metal-like Seebeck coefficient of $\geq 25\ \mu V\ K^{-1}$ [1,18,19,25,42–47,54] and carrier concentrations of the order of $\sim 10^{20}\ cm^{-3}$.[24] These findings are actually also consistent with the small gap semiconductor understanding if large intrinsic defect concentrations are considered. Half-Heusler compounds are well-known to accommodate large amounts of intrinsic defects in the cubic structure,[4,5,7–10,55] so a defect concentration of $\sim 10^{20}\ cm^{-3}$ in VFe_2Al is quite plausible especially considering V and Fe have similar chemistry but different number of valence electrons. Using a p-type carrier concentration of $10^{20}\ cm^{-3}$, and the valence band parameters derived above would correspond to a Fermi-level which lies ~0.02 eV inside the valence band. Although nominally stoichiometric VFe_2Al is intrinsically degenerately doped, charge transport at room-temperature is still bipolar (see Fig. 7) due to a very small band-gap making its Seebeck coefficient appear metal-like. The small E_g which is consistent with transport properties of the material could also result from presence of defects at elevated temperatures.[56]

 This journal is © The Royal Society of Chemistry 2020

Published on 15 July 2020. Downloaded by Northwestern University on 9/27/2020 3:50:08 AM.

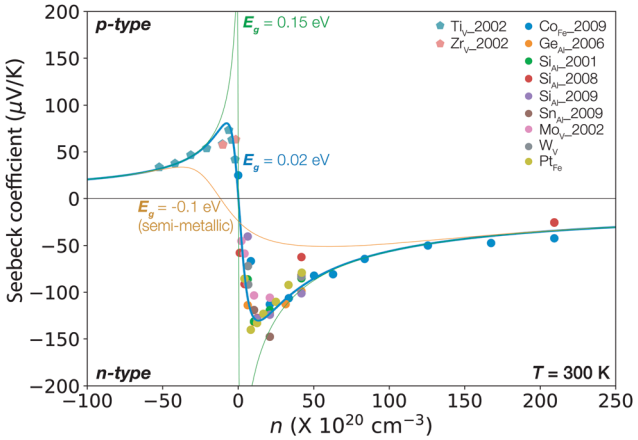

Fig. 7 Seebeck *versus* carrier concentration (n) plot of n- and p-type VFe_2Al samples (scatter points) for the entire range of carrier concentration reported in the literature.[18,19,42–47] The solid curves represent two-band acoustic phonon scattering model predictions for band-gap E_g = 0.15 eV, 0.02 eV and −0.10 eV (semimetallic). In these models, weighted mobility values of 700 $cm^2\ V^{-1}\ s^{-1}$ and 300 $cm^2\ V^{-1}\ s^{-1}$ were chosen for conduction band and valence band transport respectively. Observed Seebeck values for VFe_2Al can be best understood from a small gap semiconductor description of the compound.

2.4 Thermal modelling

As is often the case for Heusler-type compounds, pure VFe_2Al exhibits a large thermal conductivity of about 23 W m^{-1} K^{-1}, limiting its capability as a thermoelectric. However, point defect scattering of phonons has been shown to drastically reduce the lattice thermal conductivity in numerous studies of VFe_2Al with different dopants.[18,19,47,57] Fig. 8a shows the lattice thermal conductivity (κ_L) *versus* defect site fraction for Si, Ge, and Ta dopants on the Al site,[19,58] Re dopant on the Fe site, and Ti dopant on the V site.[47] The lattice thermal conductivity reduction due to point defects trends well with the Klemens alloy scattering model, which includes both the mass and site volume difference on the defect sites (see Section 4.3).[59] In most cases, there is a non-negligible contribution of the strain scattering due to the volume mismatch at the defect site. The volume difference scaling parameter (ε), which, in theory, should primarily depend on the bonding and elastic properties of the host material, is fit to the experimental data and is between 35–45 for the Si, Ge, and Ta dopant cases, which is well within the expected range for this value.[59] In contrast, the significant thermal conductivity reduction due to Re doping can be entirely explained by the large mass difference effect, while the strain scattering is negligible. Finally, Ti doping shows a minute effect on thermal conductivity as a result of its small mass and volume perturbation, and is therefore unattractive as a dopant despite the higher weighted mobility.

Finally, in some reported, sintered samples with sub-micrometer grain size, the lattice thermal conductivity is significantly reduced with undoped samples showing $\kappa_0 \sim 15$ W m^{-1} K^{-1}.[60,61] Further investigations into microstructural optimization of thermal conductivity are required in this Heusler system.[62]

We then apply the temperature-dependent model for lattice thermal conductivity discussed in Section 4.3. The umklapp and point-defect scattering effects included in the model appear to capture the measured κ_L *versus* temperature curves for varying levels of Co dopant (see Fig. 8b).[42] A single, effective Grüneisen parameter value of 2.78 was fit to the data. However, the errors in the calculation of κ_e for a narrow gap semiconductor can affect this value.

By combining this thermal transport modeling with the two-band model for electronic transport, it is then possible to treat the carrier concentration dependence of the thermoelectric figure-of-merit, $zT = S^2\sigma T/\kappa$ (Fig. 9). The n-type zT model uses the highest weighted mobility value, μ_w = 700 $cm^2\ V^{-1}\ s^{-1}$, which was found for the Ge_{Al} dopant. Ge doping on the Al site is predicted to be an effective strategy because of its minimal effect on mobility given the lack of Al character seen in electronic states around the Fermi level (see Fig. 2). Additionally, Ge_{Al} doping leads to a large thermal conductivity reduction owing to the considerable mass difference effects. On the p-type

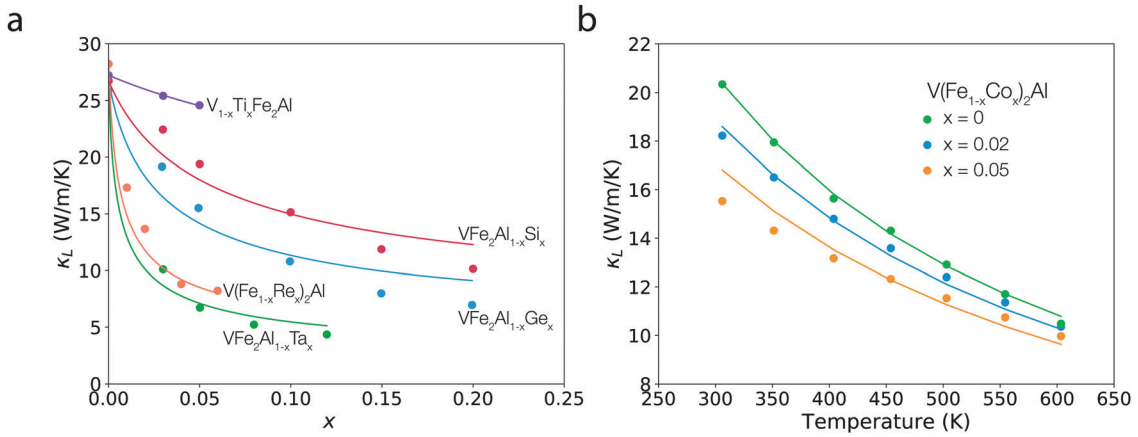

Fig. 8 κ_L trends with changes in composition are well described by analytic alloy scattering models. (a) κ_L *versus* composition curves from the literature[19,47,58] are modelled using the Klemens alloy scattering model. (b) κ_L *versus* temperature curves with varying Co dopant concentrations from Lu *et al.*[57] are modelled using point-defect and umklapp scattering theory fit with a single Grüneisen parameter of 2.78.

Published on 15 July 2020. Downloaded by Northwestern University on 9/27/2020 3:50:08 AM.

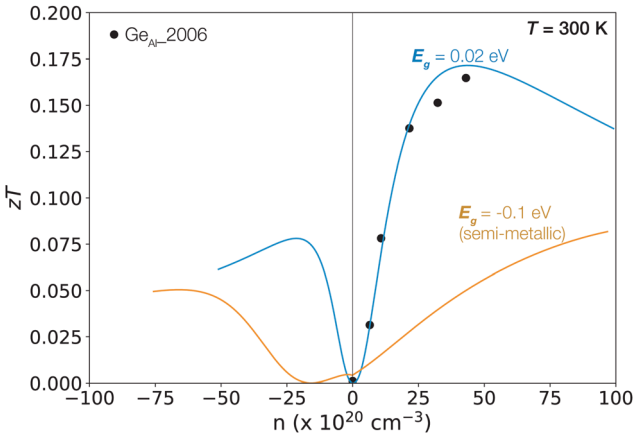

Fig. 9 The zT *versus* carrier concentration (n) curves at 300 K from a two-band model (for E_g = 0.02 eV [try 0.03] or −0.1 eV, semi-metallic) emphasize the importance of a band gap to thermoelectric performance. A max zT of 0.17 is predicted for this material at a carrier concentration of 4×10^{21} cm^{-3}. Here, the n-dependence of κ_L is included through alloy scattering using the point defect scattering strength of Ge for n-type and Re for p-type. The zT evaluation from Nishino *et al.* show good correspondence with the model.[19]

Table 1 Summary of parameters used to model the thermoelectric properties of VFe_2Al at 300 K

	E_g (eV)	μ_w (cm^2 V^{-1} s^{-1})	m^* (m_e)	Max zT	optimal n, n_{opt} (cm^{-3})	κ_L (n_{opt}) (W m^{-1} K^{-1})
n-Type	0.02	700	12.75	0.17–0.18	4×10^{21}	11.9
p-Type	0.02	300	4.7	0.08	2×10^{21}	11.3

side, we utilize the weighted mobility and thermal conductivity values for Re_{Fe} doping mainly because of the large thermal conductivity reduction observed for Re doping, again, attributed to the large mass difference at the defect site.[47]

The zT *versus* n trends (see Fig. 9) highlight the importance of having a band gap, as the semimetal example shows much lower maximum zT values that occur at very large carrier concentrations. The maximum room-temperature zT values and corresponding carrier concentrations for the true, semiconducting VFe_2Al case are listed in Table 1 (ranges express results for a range of E_g values: 0.02–0.04 eV). As suggested by the higher weighted mobility value, the n-type case shows higher thermoelectric performance. This predicted ceiling value on the zT has been experimentally probed in the Ge doping investigation, which doped up to a site fraction of $x = 0.2$,[19] and the experimental data lines up well with the two-band model prediction (Fig. 9).

3 Conclusion

VFe_2Al has drawn considerable attention as a potential inexpensive, environmentally-friendly thermoelectric, because of its large power factor, rivalling commercial n-type Bi_2Te_3, in both its bulk full-Heusler structure and its metastable, thin film form. With its intermetallic composition and metal-like properties, VFe_2Al is historically interpreted as a semimetal, despite its semiconductor-like transport properties common to thermoelectrics. Here, we show that the electronic and thermal transport model as a semiconductor explains experimental data from numerous doping studies. Our two-band electronic transport model shows that the data can only be captured by a narrow-gap semiconductor picture with $E_g \sim 0.03$ eV. The metal-like properties of undoped VFe_2Al can be rationalized with a large intrinsic defect concentration of about 10^{20} cm^{-3}.

Our analysis of dopants studied to date, points to Ge_{Al} and Re_{Fe} as the most effective n- and p-type dopants, respectively, based on their relative effects on weighted mobility and lattice thermal conductivity. Generally, the band structure and MO diagram analysis performed here points to doping on the Al site as an effective strategy owing to low Al character near the band edge. Finally, the thermal conductivity trends with composition and temperature are shown to be consistent with an analytic treatment of phonon-point-defect and umklapp phonon–phonon scattering. The temperature and carrier-concentration dependence of the zT can be determined by combining the electronic and thermal models, and predicts a maximum room-temperature n-type zT of 0.17 at $n = 4 \times 10^{21}$ cm^{-3}. Increasing the band gap through band structure engineering (*e.g.* by alloying) will have the most direct benefit to improving zT at or above room temperature. In view of the recent success of VFe_2Al as a themoelectric, our findings will be useful for optimally doping both the bulk and thin film thermoelectric materials as well as understanding the fundamental behavior of full-Heusler or metastable VFe_2Al.

4 Methods

4.1 Electronic structure calculations

First-principles density functional theory (DFT) calculations[63] were performed using Vienna *ab initio* simulation package (VASP).[64] The Perdew–Burke–Ernzerhof (PBE) exchange correlation functional used in GGA + U.[65] All calculations are performed within the projected augmented wave (PAW) method.[66] Constant $U = 0.5$ eV and $U = 1.35$ eV values are used for d-states of both V and Fe atoms respectively in the VFe_2Al structure. These values were determined by proportionally scaling down the U values obtained by Do *et al.*[38] for VFe_2Al using constrained DFT calculations ($U_{Fe} = 4$ eV, $U_V = 1.5$ eV). Plane-wave basis sets truncated at a constant energy cutoff of 350 eV were used, and Γ-centered k-point meshes with a density of ~27 500 k-points per reciprocal atom (KPPRA). All structures were relaxed with respect to cell vectors and its internal degrees of freedom until forces on all atoms were less than 0.1 eV nm^{-1}. The density of states calculations were performed using the tetrahedron method on a k-point mesh with mesh density of ~320 000 k-points per reciprocal atom (KPPRA) for both the primitive and supercell calculations. The density of states were evaluated on a grid point density of ~1000 points per eV. The Electronic structure was plotted using PYMATGEN.[67] The k-resolved Crystal Orbital Hamilton Populations (COHPs)

 This journal is © The Royal Society of Chemistry 2020

Published on 15 July 2020. Downloaded by Northwestern University on 9/27/2020 3:50:08 AM.

calculations were performed using the version 3.2.0 of the LOBSTER software.[68,69,70]

4.2 Two-band model of electrical transport

Utilizing experimental datasets from the literature, we parameterize an analytical band transport model to understand the electrical properties of VFe_2Al. Evidence of bipolar transport near room temperature and at carrier concentrations less than $\sim 10^{21}$ cm^{-3}, suggests the necessity of a two-band model capturing majority and minority carrier transport. Here, we assume carrier lifetime to be limited by acoustic phonon scattering. We first build separate effective mass models for T = 300 K transport of the conduction and valence bands, using only samples in the single-band transport regime (entered by nominally doping the compound in excess of $\sim 10^{21}$ cm^{-3} carriers). Therefore, only samples in the regime of linearly increasing $|S|$ response to temperature were chosen.

To build the transport models, data was collected from a variety of n-type (Co,[42] Si,[43–45] Ge,[19] Sn,[45] Mo,[46] Pt,[18] W[18]) and p-type (Ti,[46] Zr,[18] Re[47]) dopants used in previous thermoelectric studies. The weighted mobility – a carrier mobility parameter weighted by the density of states effective mass – is determined from thermopower ($|S|$)–conductivity (σ) relation. The weighted mobility is directly related to the thermoelectric power factor at a given doping level ($\eta = E_f/k_BT$) and temperature. Moreover, the influence of dopants on carrier mobility through effects such as alloy scattering is easy to assess *via* the weighted mobility. We also determine the Seebeck effective mass, m_s^*, which relates to the density-of-states at the Fermi level, from the $|S|$ *versus* carrier concentration (n) relation. These $|S|$–σ–n relations are detailed below through their mutual dependence on doping level η.[71] The Fermi integrals are denoted as: F_j, where j represents the order.

$$\sigma = \frac{8\pi e(2m_e k_B T)^{3/2}}{3h^3}\mu_w F_0$$
$$S = \frac{k_B}{e}\left(\frac{2F_1}{F_0} - \eta\right) \quad (1)$$
$$n = 4\pi\left(\frac{2m_s^* k_B T}{h^2}\right)^{3/2} F_{1/2}$$

Once the fitted band parameters μ_w and m_s^* have been determined for the valence and conduction band, we then build a two-band model in order to fit the band offset (E_g) that best describes the full data (*i.e.* including samples in the bipolar regime). The two band Seebeck and conductivity equations are shown below combining the electron and hole properties. Here, the relationship $\eta_p = -(E_g/(k_BT) + \eta_n)$ has been fixed when determining σ_p, S_p, and hole carrier concentration p.

$$\sigma = \sigma_p + \sigma_n \quad S = \frac{S_p\sigma_p + S_n\sigma_n}{\sigma_p + \sigma_n} \quad (2)$$

4.3 Thermal transport models

We use analytical thermal models to understand the carrier-concentration and temperature dependence of the lattice thermal conductivity. It should be noted that the lattice thermal conductivity κ_L is determined by subtracting off the electronic contribution to the thermal conductivity κ_e, which is difficult to estimate in a narrow gap semiconductor. Existing two-band models for κ_e can quickly diverge producing anomalously large values as is the case here.[71] Instead, we use the standard Wiedemann–Franz law $\kappa_e = L\sigma T$ to treat the electronic term, where the Lorentz number L is approximated as $L\,[10^{-8}\,\mathrm{W\,\Omega\,K^{-2}}] = 1.5 + \exp[-|S|/116\ \mu\mathrm{V\,K^{-1}}]$.[72]

We apply the Klemens point defect scattering model to understand the lattice thermal conductivity *versus* carrier concentration trends. The Klemens model predicts the lattice thermal conductivity ratio of the defective solid (κ_d) to that of the pure solid (κ_0) based on the disorder scaling parameter u:

$$\frac{\kappa_d}{\kappa_0} = \frac{\tan^{-1} u}{u} \quad u^2 = \frac{(6\pi^5 V_0^2)^{1/3}}{2k_B v_s}\kappa_0\Gamma. \quad (3)$$

Here, the volume per atom (V_0), lattice thermal conductivity of a reference pure solid (κ_0), and the speed of sound (v_s) are interpolated between end member values.[54] Finally, Γ is the point defect scattering parameter, which is a combination of the mass and site volume difference effects in the defective solids. In both the mass and volume terms, the scattering strength is related to the atomically averaged variance (*e.g.* $\langle\overline{\Delta M^2}\rangle$) divided by the squared atomic average (*e.g.* $\langle\overline{M}\rangle^2$). The notation below indicates two levels of averaging in each case, where site averaging on a sublattice is denoted by a bar while the final stoichiometric average of all sublattices is denoted by angular brackets $\langle\rangle$.[59]

$$\Gamma = \frac{\langle\overline{\Delta M^2}\rangle}{\langle\overline{M}\rangle^2} + \varepsilon\frac{\langle\overline{\Delta R^2}\rangle}{\langle\overline{R}\rangle^2} \quad (4)$$

The volume difference scaling parameter (ε) is treated as a phenomenological fitting parameter, but should mainly depend on the bonding and elastic properties of the host material.[73]

Additionally, we model the κ_L *versus* temperature trend by treating scattering due to point defects as well as umklapp phonon–phonon interactions.[22] The relaxation times for each process carry their own phonon frequency dependence and are additionally related to the factors which determine the scattering strength of the interaction. As discussed previously, the scattering strength of a point defect is attributed to the mass and site volume difference at the defect site. Whereas, in the Umklapp scattering case, the scattering strength is determined by the anharmoncity of the lattice as captured by the Grüneisen parameter (γ). Finally, the Debye approximation is invoked, which simplifies the phonon dispersion to $\omega = v_s k$ such that the phonon group and phase velocities are both equal to the speed of sound.

$$\tau_u = \frac{(6\pi^2)^{1/3}}{2}\frac{M_{at} v_s^3}{k_B V_{at}^{1/3}\gamma^2\omega^2 T} \quad \tau_{PD} = \frac{4\pi v_s^3}{\Gamma V_{at}\omega^4} \quad (5)$$

The relaxation times are combined using Matthiessen's rule $\tau_{tot}^{-1} = \tau_u^{-1} + \tau_{PD}^{-1}$ and incorporated in the Callaway-type expression for lattice thermal conductivity. Here, κ_L is defined

Published on 15 July 2020. Downloaded by Northwestern University on 9/27/2020 3:50:08 AM.

from a frequency integral up to the Debye frequency ω_D of the spectral heat capacity ($C_s = k_B x^2 e^x/(e^x - 1)^2$ for $x = \frac{\hbar\omega}{k_B T}$), sound velocity, and relaxation time:

$$\kappa_L = \frac{1}{3}\int_0^{\omega_D} C_s(\omega) v_s(\omega)^2 \tau(\omega) d\omega. \quad (6)$$

Conflicts of interest

There are no conflicts of interest to declare.

Acknowledgements

We acknowledge support from the U.S. Department of Energy, Office of Energy Efficiency and Renewable Energy (EERE) program ''Accelerated Discovery of Compositionally Complex Alloys for Direct Thermal Energy Conversion'' (DOE Award DE-AC02-76SF00515) and the National Science Foundation (DMREF-1729487).

Notes and references

1 T. Graf, C. Felser and S. S. P. Parkin, Simple rules for the understanding of heusler compounds, *Prog. Solid State Chem.*, 2011, **390**(1), 1–50.
2 J. Mao, Z. Liu, J. Zhou, H. Zhu, Q. Zhang, G. Chen and Z. Ren, Advances in thermoelectrics, *Adv. Phys.*, 2018, **670**(2), 69–147.
3 J. He and T. M. Tritt, Advances in thermoelectric materials research: Looking back and moving forward, *Science*, 2017, **3570**(6358), eaak9997.
4 W. G. Zeier, S. Anand, L. Huang, R. He, H. Zhang, Z. Ren, C. Wolverton and G. Jeffrey Snyder, Using the 18-electron rule to understand the nominal 19-electron half-Heusler NbCoSb with Nb vacancies, *Chem. Mater.*, 2017, **290**(3), 1210–1217.
5 S. Anand, K. Xia, V. I. Hegde, U. Aydemir, V. Kocevski, T. Zhu, C. Wolverton and G. Jeffrey Snyder, A valence balanced rule for discovery of 18-electron half-heuslers with defects, *Energy Environ. Sci.*, 2018, **110**(6), 1480–1488.
6 J. Zhou, H. Zhu, T.-H. Liu, Q. Song, R. He, J. Mao, Z. Liu, W. Ren, B. Liao and D. J. Singh, *et al.*, Large thermoelectric power factor from crystal symmetry-protected non-bonding orbital in half-heuslers, *Nat. Commun.*, 2018, **90**(1), 1–9.
7 S. Anand, M. Wood, Y. Xia, C. Wolverton and G. Jeffrey Snyder, Double half-heuslers, *Joule*, 2019, **30**(5), 1226–1238.
8 K. Xia, P. Nan, S. Tan, Y. Wang, B. Ge, W. Zhang, S. Anand, X. Zhao, G. J. Snyder and T. Zhu, Short-range order in defective half-heusler thermoelectric crystals, *Energy Environ. Sci.*, 2019, **120**(5), 1568–1574.
9 Y. Tang, X. Li, L. H. J. Martin, E. C. Reyes, T. Ivas, C. Leinenbach, S. Anand, M. Peters, G. Jeffrey Snyder and C. Battaglia, Impact of Ni content on the thermoelectric properties of half-heusler tinisn, *Energy Environ. Sci.*, 2018, **110**(2), 311–320.
10 S. Anand, K. Xia, T. Zhu, C. Wolverton and G. Jeffrey Snyder, Temperature Dependent n-Type Self Doping in Nominally 19-Electron Half-Heusler Thermoelectric Materials, *Adv. Energy Mater.*, 2018, **80**(30), 1801409.
11 S. Sakurada and N. Shutoh, Effect of Ti substitution on the thermoelectric properties of (Zr,Hf)NiSn half-heusler compounds, *Appl. Phys. Lett.*, 2005, **860**(8), 082105.
12 G. Rogl, P. Sauerschnig, Z. Rykavets, V. V. Romaka, P. Heinrich, B. Hinterleitner, A. Grytsiv, E. Bauer and P. Rogl, (V,Nb)-doped half heusler alloys based on {Ti, Zr, Hf}NiSn with high *zT*, *Acta Mater.*, 2017, **131**, 336–348.
13 C. Fu, S. Bai, Y. Liu, Y. Tang, L. Chen, X. Zhao and T. Zhu, Realizing high figure of merit in heavy-band p-type half-heusler thermoelectric materials, *Nat. Commun.*, 2015, **60**(1), 1–7.
14 H. Zhu, R. He, J. Mao, Q. Zhu, C. Li, J. Sun, W. Ren, Y. Wang, Z. Liu and Z. Tang, *et al.*, Discovery of ZrCoBi based half heuslers with high thermoelectric conversion efficiency, *Nat. Commun.*, 2018, **90**(1), 1–9.
15 H. Zhu, J. Mao, Y. Li, J. Sun, Y. Wang, Q. Zhu, G. Li, Q. Song, J. Zhou and Y. Fu, *et al.*, Discovery of TaFeSb-based half-heuslers with high thermoelectric performance, *Nat. Commun.*, 2019, **100**(1), 1–8.
16 G. Li, Q. An, U. Aydemir, W. A. Goddard III, M. Wood, P. Zhai, Q. Zhang and G. Jeffrey Snyder, Enhanced ideal strength of thermoelectric half-heusler TiNiSn by sub-structure engineering, *J. Mater. Chem. A*, 2016, **40**(38), 14625–14636.
17 M. M. Al Malki, Q. Qiu, T. Zhu, G. J. Snyder and D. C. Dunand, Creep behavior and postcreep thermoelectric performance of the n-type half-heusler alloy $Hf_{0.3}Zr_{0.7}NiSn_{0.98}Sb_{0.02}$, *Mater. Today Phys.*, 2019, **9**, 100134.
18 Y. Nishino, Development of thermoelectric materials based on Fe_2VAl Heusler compound for energy harvesting applications, *IOP Conference Series: Materials Science and Engineering*, 2011, **18**, 142001, DOI: 10.1088/1757-899×/18/14/142001.
19 Y. Nishino, S. Deguchi and U. Mizutani, Thermal and transport properties of the Heusler-type $Fe_2VAl_{1-x}Ge_x$ ($0 \leq x \leq 0.20$) alloys: effect of doping on lattice thermal conductivity, electrical resistivity, and Seebeck coefficient, *Phys. Rev. B: Condens. Matter Mater. Phys.*, 2006, **74**, 115115, DOI: 10.1103/PhysRevB.74.115115.
20 I. T. Witting, T. C. Chasapis, F. Ricci, M. Peters, N. A. Heinz, G. Hautier and G. Jeffrey Snyder, The thermoelectric properties of Bismuth Telluride, *Adv. Electron. Mater.*, 2019, **50**(6), 1800904.
21 B. Hinterleitner, I. Knapp, M. Poneder, Y. Shi, H. Müller, G. Eguchi, C. Eisenmenger-Sittner, M. Stöger-Pollach, Y. Kakefuda and N. Kawamoto, *et al.*, Thermoelectric performance of a metastable thin-film heusler alloy, *Nature*, 2019, **5760**(7785), 85–90.
22 E. S. Toberer, A. Zevalkink and G. Jeffrey Snyder, Phonon engineering through crystal chemistry, *J. Mater. Chem.*, 2011, **21**, 15843–15852, DOI: 10.1039/c1jm11754h.
23 W. G. Zeier, J. Schmitt, G. Hautier, U. Aydemir, Z. M. Gibbs, C. Felser and G. Jeffrey Snyder, Engineering half-Heusler thermoelectric materials using Zintl chemistry, *Nat. Rev. Mater.*, 2016, **10**(6), 1–10.
24 H. Okamura, J. Kawahara, T. Nanba, S. Kimura, K. Soda, U. Mizutani, Y. Nishino, M. Kato, I. Shimoyama and H. Miura,

 This journal is © The Royal Society of Chemistry 2020

Published on 15 July 2020. Downloaded by Northwestern University on 9/27/2020 3:50:08 AM.

et al., Pseudogap formation in the intermetallic compounds $(Fe_{1-x}V_x)_3Al$, *Phys. Rev. Lett.*, 2000, **840**(16), 3674.

25 C.-S. Lue and Y.-K. Kuo, Thermoelectric properties of the semimetallic Heusler compounds $Fe_{2-x}V_{1+x}M$ (M = Al, Ga), *Phys. Rev. B: Condens. Matter Mater. Phys.*, 2002, **660**(8), 085121.

26 Y. Nishino, M. Kato, S. Asano, K. Soda, M. Hayasaki and U. Mizutani, Semiconductorlike behavior of electrical resistivity in heusler-type Fe_2VAl compound, *Phys. Rev. Lett.*, 1997, **790**(10), 1909.

27 C.-S. Lue and J. H. Ross, *et al.*, Semimetallic behavior in Fe2VAl: NMR evidence, *Phys. Rev. B: Condens. Matter Mater. Phys.*, 1998, **580**(15), 9763.

28 D. J. Singh and I. I. Mazin, Electronic structure, local moments, and transport in Fe_2VAl, *Phys. Rev. B: Condens. Matter Mater. Phys.*, 1998, **570**(22), 14352.

29 R. Weht and W. E. Pickett, Excitonic correlations in the intermetallic Fe_2VAl, *Phys. Rev. B: Condens. Matter Mater. Phys.*, 1998, **580**(11), 6855.

30 G. Y. Guo, G. A. Botton and Y. Nishino, Electronic structure of possible 3d 'heavy-fermion' compound, *J. Phys.: Condens. Matter*, 1998, **100**(8), L119.

31 Kiyoshi Ooiwa and Keizo Endo, Nuclear magnetic relaxation in Heusler alloys Fe_2VGa and Fe_2VAl, *J. Magn. Magn. Mater.*, 1998, **177**, 1443–1444.

32 C.-S. Lue, J. H. Ross Jr, C. F. Chang and H. D. Yang, Field-dependent specific heat in Fe_2VAl and the question of possible 3d heavy fermion behavior, *Phys. Rev. B: Condens. Matter Mater. Phys.*, 1999, **600**(20), R13941.

33 S. S. Shastri and S. K. Pandey, A comparative study of different exchange–correlation functionals in understanding structural, electronic and thermoelectric properties of Fe_2VAl and Fe_2TiSn compounds, *Comput. Mater. Sci.*, 2018, **143**, 316–324.

34 M. Meinert, Modified Becke-Johnson potential investigation of half-metallic Heusler compounds, *Phys. Rev. B: Condens. Matter Mater. Phys.*, 2013, **870**(4), 045103.

35 D. I. Bilc, G. Hautier, D. Waroquiers, G.-M. Rignanese and P. Ghosez, Low-dimensional transport and large thermoelectric power factors in bulk semiconductors by band engineering of highly directional electronic states, *Phys. Rev. Lett.*, 2015, **1140**(13), 136601.

36 S. Sk, P. Devi, S. Singh and S. K. Pandey, Exploring the best scenario for understanding the high temperature thermoelectric behaviour of Fe_2VAl, *Mater. Res. Express*, 2018, **60**(2), 026302.

37 B. Xu, X. Li, G. Yu, J. Zhang, S. Ma, Y. Wang and L. Yi, The structural, elastic and thermoelectric properties of Fe_2VAl at pressures, *J. Alloys Compd.*, 2013, **565**, 22–28.

38 D. Do, M.-S. Lee and S. D. Mahanti, Effect of onsite coulomb repulsion on thermoelectric properties of full-heusler compounds with pseudogaps, *Phys. Rev. B: Condens. Matter Mater. Phys.*, 2011, **840**(12), 125104.

39 D. I. Bilc and P. Ghosez, Electronic and thermoelectric properties of Fe_2VAl: the role of defects and disorder, *Phys. Rev. B: Condens. Matter Mater. Phys.*, 2011, **830**(20), 205204.

40 M. Wood, K. Imasato, S. Anand, J. Yang and G. Jeffrey Snyder, The Importance of the Mg–Mg Interaction in Mg_3Sb_2–Mg_3Bi_2 Shown Through Cation Site Alloying, *J. Mater. Chem. A*, 2020, **8**, 2033–2038.

41 M. T. Dylla, A. Dunn, S. Anand, A. Jain and G. Jeffrey Snyder, *et al.*, Machine learning chemical guidelines for engineering electronic structures in half-heusler thermoelectric materials, *Research*, 2020, **2020**, 6375171.

42 W. Lu, W. Zhang and L. Chen, Thermoelectric properties of $(Fe_{1-x}Co_x)_2VAl$ Heusler-type compounds, *J. Alloys Compd.*, 2009, **4840**(1–2), 812–815.

43 H. Kato, M. Kato, Y. Nishino, U. Mizutani and S. Asano, Effect of silicon substitution on thermoelectric properties of Heusler-type Fe_2VAl alloy, *Journal of Japanese Institute of Metals*, 2001, **650**(7), 652–656.

44 M. Vasundhara, V. Srinivas and V. V. Rao, Electronic transport in Heusler-type $Fe_2VAl_{1-x}M_x$ alloys (M = B, In, Si), *Phys. Rev. B: Condens. Matter Mater. Phys.*, 2008, **770**(22), 224415.

45 E. J. Skoug, C. Zhou, Y. Pei and D. T. Morelli, High thermoelectric power factor near room temperature in full-heusler alloys, *J. Electron. Mater.*, 2009, **380**(7), 1221–1223.

46 H. Matsuura, Y. Nishino, U. Mizutani and S. Asano, Doping effects on thermoelectric properties of the pseudogap Fe_2VAl system, *Journal of Japanese Institute of Metals*, 2002, **660**(7), 767–771.

47 F. Kobayashi, N. Ide and Y. Nishino, Effects of Re Substitution on Thermoelectric Properties of Pseudogap System Fe_2VAl, *Journal of Japanese Institute of Metals*, 2007, **710**(2), 208–212.

48 A. Zevalkink, D. M. Smiadak, J. L. Blackburn, A. J. Ferguson, M. L. Chabinyc, O. Delaire, J. Wang, K. Kovnir, J. Martin, L. T. Schelhas, T. D. Sparks, S. D. Kang, M. T. Dylla, G. Jeffrey Snyder, B. R. Ortiz and E. S. Toberer, A practical field guide to thermoelectrics: fundamentals, synthesis, and characterization, *Appl. Phys. Rev.*, 2018, **50**(2), 021303, DOI: 10.1063/1.5021094URL.

49 S. D. Kang and G. Jeffrey Snyder, *Transport property analysis method for thermoelectric materials: material quality factor and the effective mass model*, 2018, pp. 1–5.

50 J. J. Kuo, S. D. Kang, K. Imasato, H. Tamaki, S. Ohno, T. Kanno and G. Jeffrey Snyder, Grain boundary dominated charge transport in Mg_3Sb_2-based compounds, *Energy Environ. Sci.*, 2018, **11**, 429–434, DOI: 10.1039/c7ee03326e.

51 H. Wang, X. Cao, Y. Takagiwa and G. J. Snyder, Higher mobility in bulk semiconductors by separating the dopants from the charge-conducting band-a case study of thermoelectric PbSe, *Mater. Horiz.*, 2015, **20**(3), 323–329.

52 S. R. Brown, E. S. Toberer, T. Ikeda, C. A. Cox, F. Gascoin, S. M. Kauzlarich and G. Jeffrey Snyder, Improved thermoelectric performance in $Yb_{14}Mn_{1-x}Zn_xSb_{11}$ by the reduction of spin-disorder scattering, *Chem. Mater.*, 2008, **200**(10), 3412–3419.

53 Z. M. Gibbs, H.-S. Kim, H. Wang and G. Jeffrey Snyder, Band gap estimation from temperature dependent Seebeck measurement—Deviations from the $2e|S_{|max}T_{max}$ relation, *Appl. Phys. Lett.*, 2015, **1060**(2), 022112.

54 C. S. Lue, Y. Kuo, S. Horng, S. Y. Peng and C. Cheng, Structural, thermal, and electronic properties of $Fe_2VSi_{1-x}Al_x$,

Published on 15 July 2020. Downloaded by Northwestern University on 9/27/2020 3:50:08 AM.

Phys. Rev. B: Condens. Matter Mater. Phys., 2005, **71**, 064202, DOI: 10.1103/PhysRevB.71.064202.

55 K. Xia, Y. Liu, S. Anand, G. J. Snyder, J. Xin, J. Yu, X. Zhao and T. Zhu, Enhanced Thermoelectric Performance in 18-Electron $Nb_{0.8}CoSb$ Half-Heusler Compound with Intrinsic Nb Vacancies, *Adv. Funct. Mater.*, 2018, **280**(9), 1705845.

56 A. Berche, M. T. Noutack, M.-L. Doublet and P. Jund, Unexpected band gap increase in the Fe_2VAl Heusler compound, *Mater. Today Phys.*, 2020, 100203.

57 W. Lu, W. Zhang and L. Chen, Thermoelectric properties of $(Fe_{1-x}Co_x)_2VAl$ Heusler-type compounds, *J. Alloys Compd.*, 2009, **484**, 812–815.

58 K. Renard, A. Mori, Y. Yamada, S. Tanaka, H. Miyazaki and Y. Nishino, Thermoelectric properties of the Heusler-type $Fe_2VTa_xAl_{1-x}$ alloys, *J. Appl. Phys.*, 2014, **115**, 033707, DOI: 10.1063/1.4861419. ISSN 00218979.

59 R. Gurunathan, R. Hanus, M. Dylla, A. Katre and G. J. Snyder, Analytical models of phonon-point-defect scattering, *Phys. Rev. Appl.*, 2020, **13**, 034011, DOI: 10.1103/PhysRevApplied.13.034011URL.

60 M. Mikami, S. Tanaka and K. Kobayashi, Thermoelectric properties of Sb-doped Heusler Fe_2VAl alloy, *J. Alloys Compd.*, 2009, **484**, 444–448, DOI: 10.1016/j.jallcom.2009.04.120.

61 M. Mikami, Y. Kinemuchi, Y. Ozaki, Y. Terazawa and T. Takeuchi, Thermoelectric properties of tungsten-substituted Heusler Fe_2VAl alloy, *J. Appl. Phys.*, 2012, **111**, 093710.

62 M. Mikami, A. Matsumoto and K. Kobayashi, Synthesis and thermoelectric properties of microstructural Heusler Fe_2VAl alloy, *J. Alloys Compd.*, 2008, **461**, 423–426, DOI: 10.1016/j.jallcom.2007.07.004. ISSN 09258388.

63 W. Kohn, A. D. Becke and R. G. Parr, Density functional theory of electronic structure, *J. Phys. Chem.*, 1996, **1000**(31), 12974–12980.

64 G. Kresse and J. Furthmüller, Efficient iterative schemes for *ab initio* total-energy calculations using a plane-wave basis set, *Phys. Rev. B: Condens. Matter Mater. Phys.*, 1996, **540**(16), 11169.

65 J. P. Perdew, K. Burke and M. Ernzerhof, Generalized gradient approximation made simple, *Phys. Rev. Lett.*, 1996, **770**(18), 3865.

66 P. E. Blöchl, Projector augmented-wave method, *Phys. Rev. B: Condens. Matter Mater. Phys.*, 1994, **500**(24), 17953.

67 S. P. Ong, W. D. Richards, A. Jain, G. Hautier, M. Kocher, S. Cholia, D. Gunter, V. L. Chevrier, K. A. Persson and G. Ceder, Python Materials Genomics (pymatgen): a robust, open-source python library for materials analysis, *Comput. Mater. Sci.*, 2013, **68**, 314–319, DOI: 10.1016/j.commatsci.2012.10.028URL.

68 R. Dronskowski and P. E. Blöchl, Crystal orbital Hamilton populations (COHP): energy-resolved visualization of chemical bonding in solids based on density-functional calculations, *J. Phys. Chem.*, 1993, **970**(33), 8617–8624.

69 V. L. Deringer, A. L. Tchougréeff and R. Dronskowski, Crystal orbital Hamilton population (COHP) analysis as projected from plane-wave basis sets, *J. Phys. Chem. A*, 2011, **1150**(21), 5461–5466.

70 S. Maintz, V. L. Deringer, A. L. Tchougréeff and R. Dronskowski, Analytic projection from plane-wave and PAW wavefunctions and application to chemical-bonding analysis in solids, *J. Comput. Chem.*, 2013, **340**(29), 2557–2567.

71 A. F. May and G. Jeffrey Snyder. *Introduction to Modeling Thermoelectric Transport at High Temperatures*, pp. 1–18. CRC Press, 2012.

72 H.-S. Kim, Z. M. Gibbs, Y. Tang, H. Wang and G. Jeffrey Snyder, Characterization of Lorenz number with Seebeck coefficient measurement, *APL Mater.*, 2015, **30**(4), 041506, DOI: 10.1063/1.4908244URL.

73 H. Wang, A. D. Lalonde, Y. Pei and G. Jeffery Snyder, The Criteria for Beneficial Disorder in Thermoelectric Solid Solutions, *Adv. Funct. Mater.*, 2012, **230**(12), 1–11, DOI: 10.1002/adfm.201201576.

 This journal is © The Royal Society of Chemistry 2020